JOURNAL OF SPACECRAFT AND ROCKETS
Vol. 30, No. 3, May–June 1993

Aerodynamic Computations for a Transonic Projectile at Angle of Attack by Total Variation Diminishing Schemes

Herng Lin* and Ching-Chang Chieng†
National Tsing Hua University, Hsinchu, Taiwan, Republic of China

Several total variation diminishing (TVD) schemes and the Beam-Warming solution algorithm have been incorporated in a computer code for solving three-dimensional time-dependent, Reynold's averaged Navier-Stokes equations in generalized coordinates. A finite-volume fully implicit, approximately factored scheme is employed with a time-step convergence acceleration. Transonic turbulent flows past a scant ogive cylinder boat tail projectile at Mach numbers 0.94 and 0.97 including base flow region were studied. Conditions at 0- and 4-deg angle of attack were computed. Results of zero angle of attack showed that third-order TVD schemes gave little improvements over the second-order TVD schemes. Van Leer's third-order MUSCL-type TVD scheme yields somewhat better results and faster convergence than Chakravarthy's upwind-biased TVD scheme. The convergence rate of the Beam-Warming scheme is similar to that of the second-order TVD schemes. The Beam-Warming scheme gives comparative results over most of the projectile except regions of coarse grids because the scheme is very sensitive to grid resolution. For angle-of-attack computations, Van Leer's third-order MUSCL-type TVD scheme still gives better agreement with measurement.

Nomenclature

$\hat{A}, \hat{B}, \hat{C}$	= flux Jacobian matrix
a	= speed of sound
C_p	= pressure coefficient
D	= projectile diameter
$\hat{E}, \hat{F}, \hat{G}, \hat{H}$	= flux vectors in transformed coordinates
J	= Jacobian
L	= dimensionless length of the body, caliber
M	= Mach number
Pr	= Prandtl number
Q	= vector of dependent variables
R_ξ, R_η, R_ζ	= right eigenvector matrix
Re	= Reynolds number; $Re_\infty \equiv \rho_\infty U_\infty D_D/\mu_\infty$
t	= time
U, V, W	= contravariant velocities in transformed coordinates
u, v, w	= dimensionless axial, normal, and circumferential velocity components
X	= distance from projectile nose along the axis of symmetry
x, y, z	= axial, normal, and circumferential coordinates
α	= differential characteristic variable vector
γ	= ratio of specific heats
$\hat{\gamma}$	= modified eigenvalues for upwind total variation diminishing (TVD)
δ_1	= small value for entropy correction function $\Psi(z)$
κ	= parameter for MUSCL-type TVD scheme
μ	= viscosity
ξ, η, ζ	= transformed coordinates
ρ	= density
ϕ	= modified flux function for upwind and symmetric TVD schemes

Subscripts

i, j, k	= located on cell centroid
$i \pm \frac{1}{2}, j \pm \frac{1}{2}, k \pm \frac{1}{2}$	= located at the cell interface
ℓ	= laminar
t	= turbulent
v	= viscous
∞	= freestream value

Superscripts

n	= time step level
T	= transpose
$\tilde{\cdot}$	= approximated numerical flux
$\hat{\cdot}$	= any variable including metric terms

Introduction

NAVIER-STOKES computations of transonic flows have been significantly advanced with the development of the implicit, approximately factored method of Beam and Warming[1] and subsequently by Pulliam and Steger.[2] It was found that the computational results by the Beam and Warming solution algorithm[3,4] can be very sensitive to a provided grid network, particularly in the complex shock/boundary-layer interaction regions. In recent years, total variation diminishing (TVD) schemes and essentially nonoscillatory (ENO) schemes have been developed to produce high resolution solutions near shocks and contact discontinuities for a wide range of multidimensional gas-dynamic problems such as the one-dimensional shock tube problem, compressible boundary-layer flow, shock/boundary-layer interaction case,[5] and flow past a real projectile.[3,4] Shiau and Hsu[3] and Hsu et al.[4] modified the Beam and Warming scheme to TVD schemes by employing more sophisticated dissipation terms and extended it to third-order-accurate resolution. Their results for the turbulent flow past a secant ogive cylinder boat-tail (SOCBT) projectile at zero angle of attack[3,4] indicated that TVD schemes could give acceptable accurate results with a rather coarse grid and save CPU time over the original Beam and Warming scheme. The aerodynamic computations for transonic projectiles at angle of attack had been performed by the flux split method,[5] symmetrical total variation diminished schemes,[6] and Beam-Warming scheme.[7,8] Only surface pressure coefficients were used for comparison with the experimental data in the cited work (except Ref. 8), which gave little proof on the improvement of the predictions for the shock/boundary-layer interaction region.

In the present work, computer programs were developed for solving two- and three-dimensional compressible Navier-Stokes equations in general curvilinear coordinates consisting

Received July 22, 1991; revision received Oct. 20, 1992; accepted for publication Oct. 20, 1992.

*Graduate Student of Power Mechanical Engineering.
†Professor of Nuclear Engineering. Member AIAA.

of options of various TVD schemes[9-12] and the Beam-Warming scheme.[1] These schemes are formulated in the finite-volume approach and incorporated in the computer programs for the inviscid terms to enhance stability and accuracy. The implicit algorithm is an approximately factored lower-upper method based on the work of Steger and Warming.[13] One objective of this study was to investigate and compare the effectiveness of these TVD schemes and the Beam-Warming scheme in solving the Navier-Stokes equations. The computations correspond to the test conditions and the model configurations given in Refs. 14 and 15. It was also noted that the computation was performed for the projectile with extended boat tail in the work of Shiau and Hsu,[6] whereas the projectile with flat base is the model for the present study. The experiment involves measurements of the surface pressure distribution and boundary-layer surveys on the afterbody of an artillery projectile based on a slightly modified version of the U.S. Army's M549 (Fig. 1). The velocity profiles near shock locations and expansion wave, as well as surface pressure coefficients, are investigated in the shock/boundary-layer interaction regions by different TVD schemes.

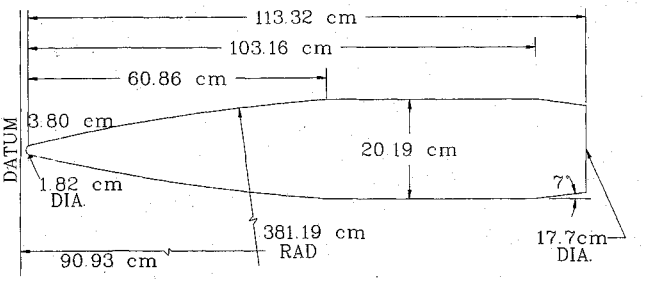

Fig. 1 Geometry of secant ogive cylinder boat-tail projectile.

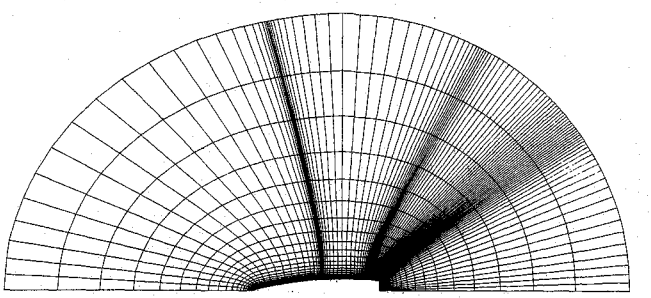

Fig. 2 105 × 50 hyperbolic O-type grid.

Governing Equations and Numerical Algorithm

Navier-Stokes Equations

The three-dimensional Reynolds-averaged Navier-Stokes equations, with the Boussinesq eddy-viscosity formulation, are written in the conservative form for the generalized coordinate system (ξ, η, ζ). The resulting equations in nondimensional form can be expressed as follows:

$$\partial_\tau(\hat{Q}) + \partial_\xi(\hat{E}) + \partial_\eta(\hat{F}) + \partial_\zeta(\hat{G}) = \partial_\xi(\hat{E}_v) + \partial_\eta(\hat{F}_v) + \partial_\zeta(\hat{G}_v) \quad (1)$$

where ξ, η, and ζ are coordinates in the longitudinal, near normal, and circumferential directions, respectively, τ is the time, and

$$\hat{Q} = J^{-1}[\rho, \rho u, \rho v, \rho w, e]^T$$

$$\hat{E} = J^{-1}[\rho U, \rho uU + \xi_x p, \rho vU + \xi_y p, \rho wU + \xi_z p, U(e+p)]^T$$

$$\hat{F} = J^{-1}[\rho V, \rho uV + \eta_x p, \rho vV + \eta_y p, \rho wV + \eta_z p, V(e+p)]^T$$

$$\hat{G} = J^{-1}[\rho W, \rho uW + \zeta_x p, \rho vW + \zeta_y p, \rho wW + \zeta_z p, W(e+p)]^T$$

$$\hat{E}_v = (M_\infty/Re_\infty)J^{-1}[E_{v1}, E_{v2}, E_{v3}, E_{v4}, E_{v5}]^T$$

$$\hat{F}_v = (M_\infty/Re_\infty)J^{-1}[F_{v1}, F_{v2}, F_{v3}, F_{v4}, F_{v5}]^T$$

$$\hat{G}_v = (M_\infty/Re_\infty)J^{-1}[G_{v1}, G_{v2}, G_{v3}, G_{v4}, G_{v5}]^T$$

where

$$U = \xi_x u + \xi_y v + \xi_z w, \quad V = \eta_x u + \eta_y v + \eta_z w, \quad W = \zeta_x u + \zeta_y v + \zeta_z w, \quad E_{v1} = 0, \quad E_{v2} = \tau_{xx}\xi_x + \tau_{xy}\xi_y + \tau_{xz}\xi_z$$

$$E_{v3} = \tau_{xy}\xi_x + \tau_{yy}\xi_y + \tau_{yz}\xi_z, \quad E_{v4} = \tau_{xz}\xi_x + \tau_{yz}\xi_y + \tau_{zz}\xi_z, \quad E_{v5} = uE_{v2} + vE_{v3} + wE_{v4} + (\gamma-1)^{-1}\Gamma_{\text{eff}}[g_1(a^2)_\xi + g_2(a^2)_\eta + g_3(a^2)_\zeta]$$

$$F_{v1} = 0, \quad F_{v2} = \tau_{xx}\eta_x + \tau_{xy}\eta_y + \tau_{xz}\eta_z, \quad F_{v3} = \tau_{xy}\eta_x + \tau_{yy}\eta_y + \tau_{yz}\eta_z, \quad F_{v4} = \tau_{xz}\eta_x + \tau_{yz}\eta_y + \tau_{zz}\eta_z, \quad F_{v5} = uF_{v2} + vF_{v3} + wF_{v4}$$

$$+ (\gamma-1)^{-1}\Gamma_{\text{eff}}[g_4(a^2)_\xi + g_5(a^2)_\eta + g_6(a^2)_\zeta], \quad G_{v1} = 0, \quad G_{v2} = \tau_{xx}\zeta_x + \tau_{xy}\zeta_y + \tau_{xz}\zeta_z, \quad G_{v3} = \tau_{xy}\zeta_x + \tau_{yy}\zeta_y + \tau_{yz}\zeta_z$$

$$G_{v4} = \tau_{xz}\zeta_x + \tau_{yz}\zeta_y + \tau_{zz}\zeta_z, \quad G_{v5} = uG_{v2} + vG_{v3} + wG_{v4} + (\gamma-1)^{-1}\Gamma_{\text{eff}}[g_7(a^2)_\xi + g_8(a^2)_\eta + g_9(a^2)_\zeta], \quad \Gamma_{\text{eff}} = \mu_l/Pr_l + \mu_t/Pr_t$$

$$g_1 = \xi_x^2 + \xi_y^2 + \xi_z^2, \quad g_2 = \xi_x\eta_x + \xi_y\eta_y + \xi_z\eta_z, \quad g_3 = \xi_x\zeta_x + \xi_y\zeta_y + \xi_z\zeta_z, \quad g_4 = \xi_x\eta_x + \xi_y\eta_y + \xi_z\eta_z, \quad g_5 = \eta_x^2 + \eta_y^2 + \eta_z^2$$

$$g_6 = \zeta_x\eta_x + \zeta_y\eta_y + \zeta_z\eta_z, \quad g_7 = \xi_x\zeta_x + \xi_y\zeta_y + \xi_z\zeta_z, \quad g_8 = \zeta_x\eta_x + \zeta_y\eta_y + \zeta_z\eta_z, \quad g_9 = \zeta_x^2 + \zeta_y^2 + \zeta_z^2, \quad \tau_{xx} = \tfrac{2}{3}\mu_{\text{eff}}(2u_x - v_y - w_z)$$

$$\tau_{xy} = \mu_{\text{eff}}(u_y + v_x), \quad \tau_{xz} = \mu(u_z + w_x), \quad \tau_{yy} = \tfrac{2}{3}\mu_{\text{eff}}(2v_y - u_x - w_z), \quad \tau_{yz} = \mu_{\text{eff}}(v_z + w_y), \quad \tau_{zz} = \tfrac{2}{3}\mu_{\text{eff}}(2w_z - u_x - v_y)$$

The diffusive coefficient μ_{eff} consists of molecular and turbulent parts (i.e., $\mu_{\text{eff}} = \mu_l + \mu_t$). The turbulent eddy viscosity is modeled by the Baldwin and Lomax[16] algebraic formulation.

Numerical Algorithm

A finite-volume approach is used for discretizing the three-dimensional governing equations, i.e., the numerical fluxes are defined at cell interfaces and the dependent variables are defined at the centroids. The finite difference formulation of Eq. (1) can be formulated as

$$\hat{Q}_{i,j,k}^{n+1} - \hat{Q}_{i,j,k}^{n} = -\frac{\Delta t}{\Delta\xi}[(\tilde{E} - \tilde{E}_v)_{i+\frac{1}{2},j,k} - (\tilde{E} - \tilde{E}_v)_{i-\frac{1}{2},j,k}]^{n+1}$$

$$- \frac{\Delta t}{\Delta\eta}[(\tilde{F} - \tilde{F}_v)_{i,j+\frac{1}{2},k} - (\tilde{F} - \tilde{F}_v)_{i,j-\frac{1}{2},k}]^{n+1}$$

$$- \frac{\Delta t}{\Delta\zeta}[(\tilde{G} - \tilde{G}_v)_{i,j,k+\frac{1}{2}} - (\tilde{G} - \tilde{G}_v)_{i,j,k-\frac{1}{2}}]^{n+1} \quad (2)$$

When evaluating the numerical flux functions $\tilde{E}_{i\pm\frac{1}{2},j,k}$, the metrics are evaluated at $i \pm \frac{1}{2}, j, k$. Likewise, the metrics are evaluated at $i, j \pm \frac{1}{2}, k$ for $\hat{F}_{i,j\pm\frac{1}{2},k}$ or $i, j, k \pm \frac{1}{2}$ for $\hat{G}_{i,j\pm\frac{1}{2},k}$. In this study, TVD schemes are employed for three-dimensional and two-dimensional computations. The expressions of the numerical fluxes for the schemes adopted in the present three-dimensional computations are described briefly here (in the ξ direction) and the details can be found in the cited references. The numerical flux expressions for two-dimensional computations are given in Refs. 10 and 11 and are not repeated in this paper.

Van Leer's Third-Order MUSCL-Type Total Variation Diminishing Scheme[9]

The numerical flux can be written in terms of

$$\tilde{E}_{i+\frac{1}{2},j,k} = \tfrac{1}{2}[\hat{E}(Q^R_{i+\frac{1}{2},j,k}) + \hat{E}(Q^L_{i+\frac{1}{2},j,k}) - \hat{R}_{i+\frac{1}{2},j,k}|\hat{\lambda}|_{i+\frac{1}{2},j,k}\hat{\alpha}_{i+\frac{1}{2},j,k}] \tag{3}$$

where

$$Q^L_{i+\frac{1}{2},j,k} = Q_{i,j,k} + \frac{s}{4}[(1-\kappa s)(\Delta Q)^- + (1+\kappa s)(\Delta Q)^+]_{i,j,k}$$
$$Q^R_{i-\frac{1}{2},j,k} = Q_{i,j,k} - \frac{s}{4}[(1-\kappa s)(\Delta Q)^+ + (1+\kappa s)(\Delta Q)^-]_{i,j,k} \tag{4}$$

and where

$$(\Delta Q)^-_{i,j,k} = Q_{i,j,k} - Q_{i-1,j,k}$$
$$(\Delta Q)^+_{i,j,k} = Q_{i+1,j,k} - Q_{i,j,k}$$
$$s = [2(\Delta Q)^-_{i,j,k}(\Delta Q)^+_{i,j,k} + \epsilon_0]/[(\Delta Q)^{-2}_{i,j,k}(\Delta Q)^{+2}_{i,j,k} + \epsilon_0]$$
$$\kappa = \tfrac{1}{3} \quad \text{for third-order scheme}$$
$$\epsilon_0 = 1.0E-6$$

The Roe's average method[17] is used to calculate the right-eigenvector matrix $\hat{R}_{i+\frac{1}{2},j,k}$, its inverse $\hat{R}^{-1}_{i+\frac{1}{2},j,k}$, and the eigenvalues $|\hat{\lambda}|_{i+\frac{1}{2},j,k}$. The differential characteristic (Riemann) variable matrix is defined as $\hat{\alpha}_{i+\frac{1}{2},j,k} = \hat{R}^{-1}_{i+\frac{1}{2},j,k}(Q^R_{i+\frac{1}{2},j,k} - Q^L_{i+\frac{1}{2},j,k})$. This scheme will display third-order accuracy in the smooth region but is reduced to first-order accuracy near shock or other extreme value regions.

For the case of angle of attack, a modified limiter by Ref. 18 is implemented for evaluating the interface state variable $Q^L_{i+\frac{1}{2},j,k}$ and $Q^R_{i-\frac{1}{2},j,k}$ as Van Leer's MUSCL-type TVD scheme is employed; i.e.,

$$Q^L_{i+\frac{1}{2},j,k} = Q_{i,j,k} + (Q_{i+1,j,k} - Q_{i-1,j,k})\tilde{Q}^L_f$$
$$Q^R_{i-\frac{1}{2},j,k} = Q_{i,j,k} - (Q_{i+1,j,k} - Q_{i-1,j,k})\tilde{Q}^R_f \tag{5}$$

where $\tilde{Q}^L_f$ and $\tilde{Q}^R_f$ are normalized interface variables and evaluated by the monotonic functions as follows:

$$\tilde{Q}^L_f = \tilde{Q}^L_C[\tilde{Q}^L_C - S_\infty\beta_1]/(\tilde{Q}^L_C - \beta_1) \quad \text{for} \quad \tilde{Q}^L_C \le 0 \tag{6a}$$

$$\tilde{Q}^L_f = (10-4S_\infty)\tilde{Q}^{L^4}_C + (8S_\infty - 19)\tilde{Q}^{L^3}_C + (10-5S_\infty)\tilde{Q}^{L^2}_C + S_\infty\tilde{Q}^L_C \quad \text{for} \quad 0 \le \tilde{Q}^L_C \le 1 \tag{6b}$$

$$\tilde{Q}^L_f = 1 + (\tilde{Q}^L_C - 1)[\tilde{Q}^L_C - 1 + (3-S_\infty)\beta_1]/(\tilde{Q}^L_C - 1 + \beta_1) \quad \text{for} \quad \tilde{Q}^L_C \ge 1 \tag{6c}$$

The normalized variables $\tilde{Q}^L_C$ and $\tilde{Q}^R_C$ are defined as

$$\tilde{Q}^L_C = (Q_{i,j,k} - Q_{i-1,j,k})/(Q_{i+1,j,k} - Q_{i-1,j,k})$$
$$\tilde{Q}^R_C = (Q_{i,j,k} - Q_{i+1,j,k})/(Q_{i-1,j,k} - Q_{i+1,j,k})$$

where β_1 and S_∞ are constants and are set equal to 0.05 and 2.0, respectively.

This modified limiter is third order, continuously differentiable, and exhibits greater merit than Van Leer's original smooth limiter [Eq. (4)] for the MUSCL procedure. For the MUSCL procedure, if the interpolation of some cell-center values is nonmonotonic, then the accuracy is expected to reduce to first order and the nonphysical interpolative value can be avoided. In this study, it is found that Van Leer's smooth limiter still generates some nonphysical cell interface values of dependent variable, if the variations of these node values are nonmonotonic at some location. The limiter of Eqs. (6) eliminates this problem and is chosen for the computation of the case of the angle of attack. Because this limiter requires more computer time than Van Leer's smooth limiter does, it is only incorporated in the longitudinal direction.

Yee's Second-Order-Symmetric Total Variation Diminishing Scheme[12]

The numerical flux function $\tilde{E}_{i+\frac{1}{2},j,k}$ is defined as

$$\tilde{E}_{i+\frac{1}{2},j,k} = \tfrac{1}{2}[\hat{E}_{i,j,k} + \hat{E}_{i+1,j,k} + \hat{R}_{i+\frac{1}{2},j,k}\hat{\phi}_{i+\frac{1}{2},j,k}] \tag{7}$$

where

$$\hat{\phi}_{i+\frac{1}{2},j,k} = -\Psi(\hat{\lambda}_{i+\frac{1}{2},j,k})(\hat{\alpha}_{i+\frac{1}{2},j,k} - \hat{W}_{i+\frac{1}{2},j,k})$$
$$\hat{W}_{i+\frac{1}{2},j,k} \equiv \text{minmod}(\hat{\alpha}_{i-\frac{1}{2},j,k}, \hat{\alpha}_{i+\frac{1}{2},j,k}, \hat{\alpha}_{i+3/2,j,k})$$
$$\Psi(z) = |z| \qquad |z| \ge \delta_1$$
$$= (z^2 + \delta_1^2)/2\delta_1 \qquad |z| < \delta_1$$

This scheme is a non-MUSCL-type second-order TVD scheme and is also called a "modified flux scheme." The value of δ_1 is set equal to 0.05 in the present computation. The "minimod" function of a list of arguments is equal to the smallest number in absolute value of the list of arguments is of the same sign, or is equal to zero if any arguments are opposite sign. The function $\Psi(z)$ is an entropy correction to z. $\hat{E}_{i,j,k}$ and $\hat{E}_{i+1,j,k}$ are evaluated with metrics computed at $i+\frac{1}{2}, j, k$. $\hat{R}_{i+\frac{1}{2},j,k}$ is the matrix of right eigenvectors of the Jacobian matrix $\partial\hat{E}/\partial\hat{Q}$ evaluated using Roe's averaged variables, and $\hat{\phi}$ is a vector that contains the first-order diffusion and second-order correction times.

Beam and Warming Second-Order Scheme[1]

The numerical flux $\tilde{E}_{i+\frac{1}{2},j,k}$ can be defined as

$$\tilde{E}_{i+\frac{1}{2},j,k} = \tfrac{1}{2}(\hat{E}_{i,j,k} + \hat{E}_{i+1,j,k} - \hat{D}_{i+\frac{1}{2},j,k}) \tag{8}$$

where $\hat{D}_{i+\frac{1}{2},j,k}$ is the dissipative flux. The coefficients of $\hat{D}_{i+\frac{1}{2},j,k}$ can be used to turn on the second-order and turn off the fourth-order difference terms near a shock. $\hat{D}_{i+\frac{1}{2},j,k}$ is given as

$$\hat{D}_{i+\frac{1}{2},j,k} = J^{-1}(U + C|\overline{\nabla}_\xi|)\cdot[\chi_2\cdot\max(\nu_i, \nu_{i+1})(Q_{i+1,j,k} - Q_{i,j,k}) - \frac{1}{2+\chi_2(\nu_i+\nu_{i+1})}(Q_{i+2,j,k} - 3Q_{i+1,j,k} + 3Q_{i,j,k} - Q_{i-1,j,k})] \tag{9}$$

where

$$\nu_i \equiv \frac{|p_{i+1,j,k} - 2p_{i,j,k} + p_{i-1,j,k}|}{|p_{i+1,j,k} + 2p_{i,j,k} + p_{i-1,j,k}|}$$

$$\chi_2 \equiv \epsilon_2(12 + 8M_\infty)$$

ϵ_2 is chosen as 0.8 in the present study. U is the contravariant velocity ($U \equiv \xi_x u + \xi_y v + \xi_z w$) and C is the local speed of sound.

It must be noted that these schemes differ from the original Beam-Warming scheme by using the finite volume approach, and better convergence characteristics are expected.

Viscous Terms

The TVD schemes adopted in the present study are originally designed for the inviscid Euler equations. However, this study is proposed to investigate the effectiveness of these schemes for the viscous flow problem. Therefore, a second-order-accurate, central differencing scheme is used for the viscous term along with all TVD schemes adopted in the present study.

Time Differencing

The implicit algorithm is basically a backward Euler time-integration scheme that uses lower-upper approximate factorization in delta form as suggested by Steger and Warming,[13] i.e.,

$$[I + \Delta t(\partial_\xi^- \hat{A}^+ + \partial_\eta^- \hat{B}^+ + \partial_\zeta \hat{C}^+)]^n [I + \Delta t(\partial_\xi^+ \hat{A}^- + \partial_\eta^+ \hat{B}^- + \partial_\zeta^+ C^-)]^n (\Delta \hat{Q})^n_{i,j,k} = [\text{RHS of Eq. (2)}]^n \tag{10}$$

where the splitting Jacobian matrices $\hat{A}^+$, $\hat{A}^-$, $\hat{B}^+$, $\hat{B}^-$, $\hat{C}^+$, and $\hat{C}^-$ are evaluated by model matrices $\hat{R}_\xi$, $\hat{R}_\eta$, and $\hat{R}_\zeta$ and diagonal matrices $[\hat{\lambda}_\xi^\pm]$, $[\hat{\lambda}_\eta^\pm]$, and $[\hat{\lambda}_\zeta^\pm]$, i.e.,

$$\hat{A}^+ = \hat{R}_\xi[\hat{\lambda}_\xi^+]\hat{R}_\xi^{-1}, \qquad \hat{A}^- = \hat{R}_\xi[\hat{\lambda}_\xi^-]\hat{R}_\xi^{-1} \tag{11}$$

and a similar form for $\hat{B}^+$, $\hat{B}^-$, $\hat{C}^+$, $\hat{C}^-$. $[\hat{\lambda}_\xi^\pm]$, $[\hat{\lambda}_\eta^\pm]$, and $[\hat{\lambda}_\zeta^\pm]$ are diagonal matrices whose elements are all positive and all negative eigenvalues.

Generally, to maintain the stability of the thin-layer viscous term, the split Jacobian matrices $\hat{A}^\pm$ (or $\hat{B}^\pm$, $\hat{C}^\pm$) are modified as follows[19]:

$$\hat{A}^\pm = \hat{R}_\xi([\hat{\lambda}_\xi^\pm] \pm \nu \hat{I})\hat{R}_\xi^\pm$$

where

$$\nu = \frac{2\gamma M_\infty(\mu_{\text{eff}}/\rho)\,|\overline{\nabla}\xi|^2}{(Re\,Pr)} \tag{12}$$

These Jacobian matrices ($\hat{A}^\pm$, $\hat{B}^\pm$, $\hat{C}^\pm$) are evaluated at cell interfaces.

If one is interested in the steady-state solution only, then the time step Δt can be allowed to change from location to location. The use of space varying Δt can be interpreted as an attempt to use a more uniform Courant number through the flowfield. Changing Δt can be effective for grid spacings that vary from very fine to very coarse. For subsonic and transonic flows, a purely geometric variation Δt is adequate.[20] The formula for space varying time step Δt in the finite-volume discretization can be given as

$$\Delta t = \frac{\Delta t_{\text{ref}}}{1 + \sqrt{J}}$$

Generation of the Computational Grid

Numerical results by the TVD schemes and the Beam-Warming scheme are presented to illustrate the performance and their convergence acceleration of the Navier-Stokes solver of this study. One test problem is chosen as transonic turbulent flows past a secant ogive cylinder boat-tail projectile. The calculated results are compared with experimental data.[14,15] The projectile model as shown in Fig. 1 has a 3-caliber secant ogive part (or nose part) followed by a 2.3-caliber cylinder and 0.5-caliber 7-deg boat tail. In this study the computational grid (O type) is established by using the hyperbolic solver.[21] The outer boundary of the flow domain is about 18 calibers from the projectile and an exponential stretching function with minimum spacing of 0.00002 caliber from the solid boundary in the hyperbolic grid generations, which provides 2–3 grid points in the viscous sublayer. Figure 2 shows the grid system of 105×50 points. The boundary grid points are distributed as 1-23-50-89-105 for secant ogive, cylinder, boat tail, and base region.

For the 4-deg angle-of-attack problem, the computational grid system of $108 \times 60 \times 20$ points is an O-type grid. The three-dimensional O-type grid is established by rotating the 108×60 O-type planar grid about the axis of the projectile from the azimuthal angle 0–180 deg at 19 nonconstant intervals (i.e., 7–10 deg). Figure 3 shows the planar grid system of 108×60 points. The boundary grid points are distributed as 1-23-39-79-108 for secant ogive, cylinder, boat tail, and base region.

Boundary Conditions

For a projectile of zero angle of attack, symmetry boundary conditions are used at the first and the last ξ-grid lines for the O-type grid network. The state variables and contravariant velocities at these two symmetric lines are obtained by the characteristic extrapolation from the interior control points. The same extrapolating technique is applied at the far-field inflow and outflow positions (i.e., $\eta = \eta_{\max}$). The convergence of the present Navier-Stokes solver is faster by this method than by setting a constant of freestream value at the far-field boundary. A no-slip boundary condition is adopted on the projectile surface for velocities u and v. The density and pressure on the wall are set to be equal to the values of node points next to the wall. It is assumed that the normal momentum equation suggested by Pulliam and Steger[2] need not be solved because the point of $J = 2$ is very close to the wall compared to the grid space in the longitudinal direction.

For the three-dimensional case of the O-type grid network, the boundary conditions in longitudinal ξ and normal η directions are similar to those of the two-dimensional case and only half of the projectiles are solved due to symmetry. The state variables are obtained by first-order extrapolation and the noflow condition (i.e., $w = 0$) is applied at the symmetric plane.

Convergence Acceleration

The time step $(\Delta t)_{\text{ref}}$ for the first several time steps (say, m steps) is a constant which is selected to be equal to 1.0 for the 0-deg angle of attack case and 0.7 for the 4-deg angle of attack case. The L_2 residual is calculated for each time step and is taken as a reference value for extending the time step. After m time steps, the time step $(\Delta t)_{\text{ref}}$ is changed in every time step and calculated by the formula

$$(\Delta t)^n_{\text{ref}} = \frac{-(\log_{10}\|R\|_2^n - \log_{10}\|R\|_2^m)}{3} T_\alpha + 1.0$$

where $\|R\|_2^n$ is the L_2 residual of the specific iteration, $\|R\|_2^m$ is the L_2 residual of the mth iteration, and T_α the proportional factor which is chosen as 2 in this study. For the two-dimen-

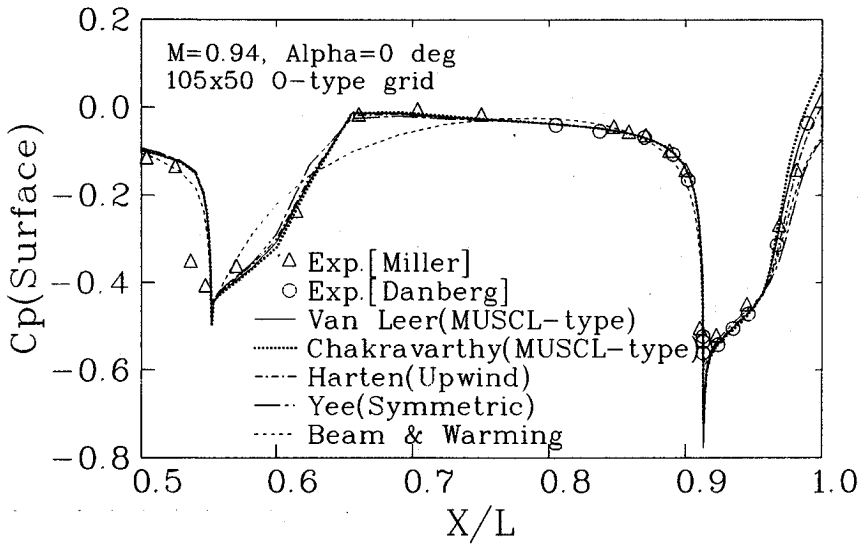

Fig. 3 108 × 60 hyperbolic O-type grid.

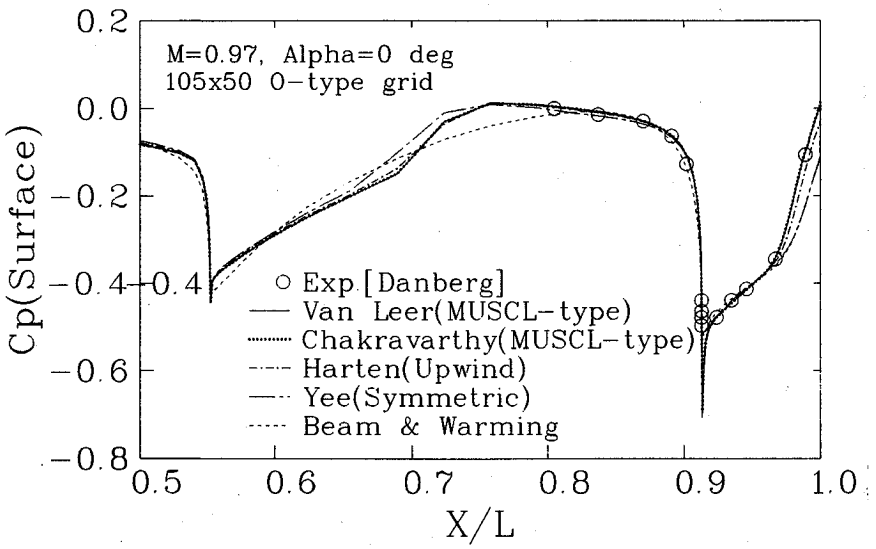

Fig. 4 Surface pressure coefficient distributions by different schemes, $M_\infty = 0.94$, $\alpha = 0$ deg.

sional case, m is selected as 80 and for three-dimensional case m is 160.

Results and Discussion

0-Deg Angle of Attack

The four TVD schemes used for comparison in the case of zero angle of attack are 1) Van Leer's third-order MUSCL-type TVD scheme,[9] 2) Chakravarthy's third-order MUSCL-type TVD scheme,[10] 3) Harten's second-order upwind TVD scheme,[11] and 4) Yee's second-order symmetric TVD scheme.[12]

Surface Pressure Coefficient

The computed surface pressure coefficients along the projectile C_p for Mach numbers 0.94 and 0.97 are compared with the experimental data[14-15] as shown in Figs. 4 and 5, respectively. For Mach number 0.94, the computed values by TVD schemes agree with experimental data except at $X/L = 0.525$–0.537. Speaking overall, all TVD schemes yield very similar results except at the nose-cylinder junction and in the boat tail near the base region. The symmetric TVD scheme (second-order accurate) exhibits large difference at $X/L = 0.63$ and $X/L \cong 1.0$ where the static pressure rises sharply. The figures show that the third-order schemes provide little improvement over the second-order schemes in this problem. Harten's upwind scheme gives better agreement with data than Yee's symmetric scheme, although both schemes are second-order accurate. For Mach number 0.97 (Fig. 5), the experimental data are only available at $0.8 < X/L < 1.0$ and the comparisons of computational result by different TVD

schemes are similar to the trends of Mach number 0.94. The computed result by the symmetric TVD scheme is the worst prediction among all schemes, especially near the end of the boat tail. The nonsmoothness near $X/L = 0.7$ is caused by the coarse grids distributed in this region.

Velocity Profile

The velocity profiles at various axial positions for Mach numbers 0.94 and 0.97 are shown in Figs. 6 and 7, respectively. For a Mach number of 0.94, the four TVD schemes exhibit excellent agreement with experimental data at stations $X/L = 0.902$, 0.946, and 0.989, but overestimate the velocity magnitude at $X/L = 0.967$. The discrepancy at this station ($X/L = 0.967$) may be caused by the difficulty of measurement[8] near the shock wave (referred to the Mach number contours shown in Fig. 8). The disagreement at $X/L = 0.924$ is related to errors in the reduced measurement data, and the details were discussed in Ref. 10. For the station $X/L = 0.989$, three of the four schemes yield very good predictions of the velocity profile and overestimation is observed by the symmetric TVD scheme. The trends can also be implied by the surface pressure coefficient at these axial locations by Fig. 4. It is noted that Van Leer's MUSCL-type and Chakravarthy's MUSCL-type schemes are third-order accurate, and Harten's upwind scheme and Yee's symmetric scheme are second-order accurate. It is found that the symmetric TVD scheme is more easily reduced to a lower-order-accurate scheme near the shock location than the upwind TVD scheme, which is obtained by examining the modified numerical fluxes of dependent variables. Therefore, Yee's symmetric TVD scheme yields the worst surface pressure coefficient and velocity profiles among these four schemes for positions near the shock wave. The third-order schemes offer very small improvement on the prediction of velocity profiles over second-order schemes. For Mach number 0.97 (Fig. 7), all four schemes show excellent agreement with measurement results at stations $X/L = 0.87$, 0.946, and 0.967 but yield different predictions at the stations $X/L = 0.924$ and 0.989. The shock wave location (which can be seen from the Mach number contours of Fig. 9) is close to the corner of the boat tail and base, near $X/L = 0.989$; therefore some discrepancies between measurement and computa-

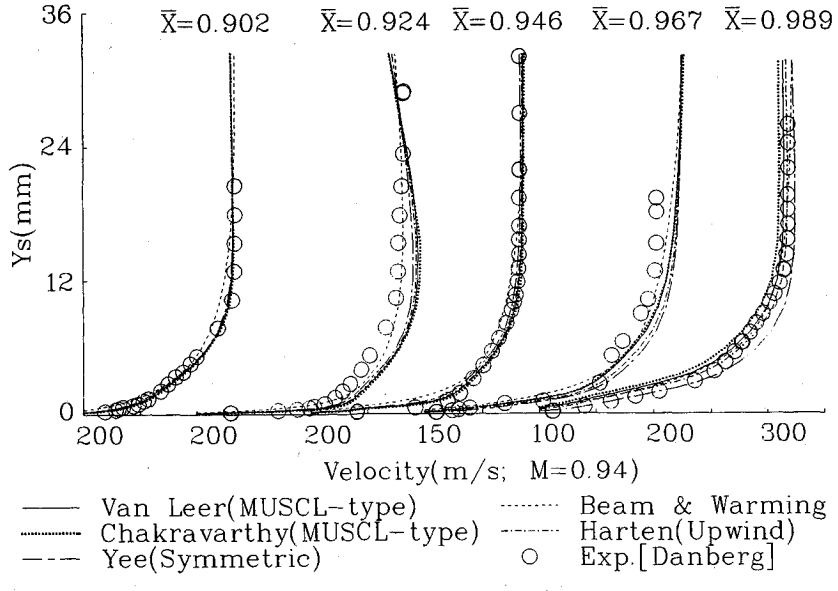

Fig. 5 Surface pressure coefficient distributions by different schemes, $M_\infty = 0.97$, $\alpha = 0$ deg.

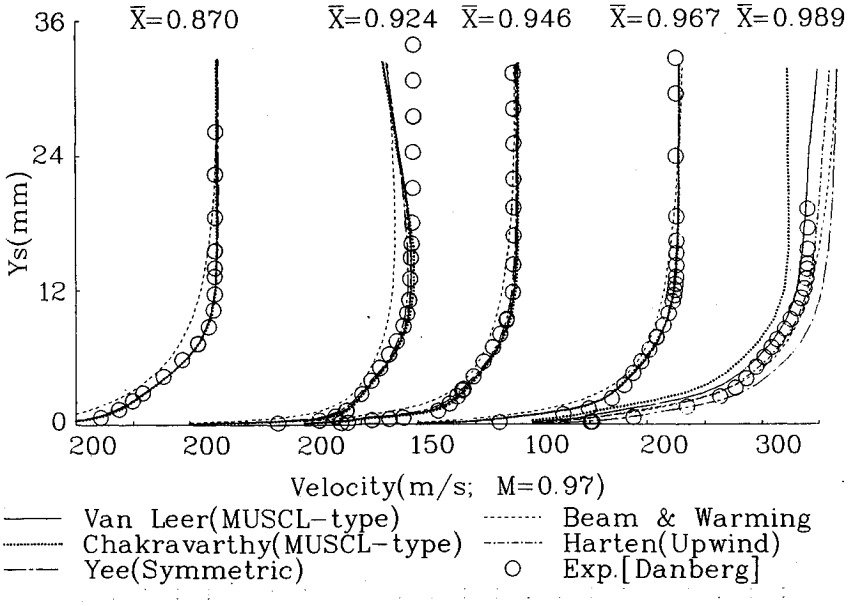

Fig. 6 Velocity profiles at various axial station, $M_\infty = 0.94$, $\alpha = 0$ deg.

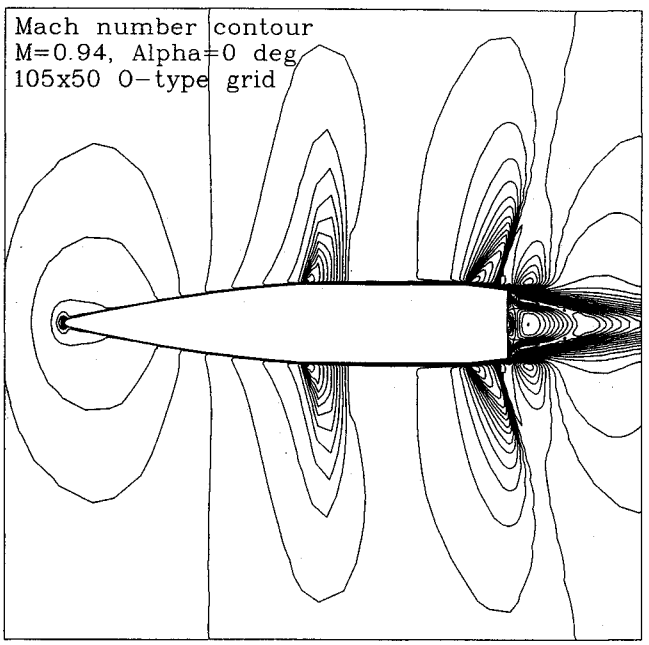

Fig. 7 Velocity profiles at various axial stations, $M_\infty = 0.97$, $\alpha = 0$ deg.

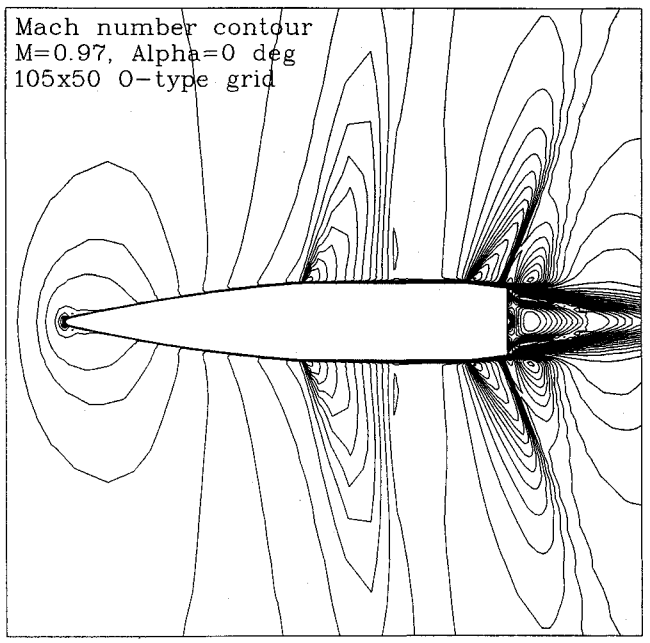

Fig. 8 Mach number contour, $M_\infty = 0.94$, $\alpha = 0$ deg.

tion are found only at this station. Figures 5 and 7 also indicate that Yee's symmetric TVD scheme gives the worst agreement among the four TVD schemes.

Iteration History

The iteration histories for the four TVD schemes are plotted in Figs. 10 and 11. It is found that the convergent rate of Yee's symmetric TVD scheme is the fastest although a very small magnitude oscillation after iteration number 700 is observed for Mach number 0.94. The fast convergence is expected because it is a lower-order-accurate scheme. The convergent rate by Chakravarthy's scheme is the slowest and the residual cannot be further reduced after 520 iterations. The iteration histories of Van Leer's MUSCL-type scheme and Harten's scheme are very close for Mach number 0.94 before iteration number 600 but the residual by Van Leer's scheme goes up again after the residual is already reduced to 10^{-7}. Figure 11 shows that the iteration histories are slightly different for Mach number 0.97 and 0.94. Yee's symmetric scheme experiences the fastest convergence among the four schemes. Harten's upwind and Van Leer's MUSCL-type TVD schemes yield close iteration histories for Mach number 0.97. It is also noted that the present program exhibits better convergence than previous work, i.e., the L_2 residual can be reduced to six order in the present work, less than three orders lower than in previous work.[22]

Comparisons Between TVD and Beam-Warming Schemes

The Beam-Warming scheme is also implemented in the computer program as an option and comparisons with other TVD schemes are studied. The computations are performed by the same computational grid and same program by Beam-Warming numerical flux [Eq. (8)]. Figure 4 shows that the Beam-Warming scheme yields good agreement with experimental data and TVD schemes at $0.750 < X/L < 0.967$, poor agreement at the nose-cylinder junction, and computational results with Yee's symmetric scheme. The coarse grids at the nose-cylinder junction give very poor results by the Beam-Warming scheme but satisfactory results by the TVD schemes. It is confirmed that results obtained using the Beam-Warming scheme are sensitive to the coarse grid. The predicted velocities by the Beam-Warming scheme are somewhat lower than that by the TVD schemes at all stations except at $X/L = 0.989$, which is the closest station to the base corner for Mach numbers 0.94 and 0.97 (Figs. 6 and 7). The convergence rate by this scheme is comparable with TVD second-order schemes (Figs. 10 and 11).

CPU Time

The two-dimensional computations were performed on the CRAY XMP-14 computer. The 105×50 grid required 0.3×10^6 words of memory storage. Table 1 shows the CPU time for the five schemes. This table indicates that the CPU time per iteration per grid point by the Beam-Warming scheme is the shortest in the present formulation, but it is only 3% shorter

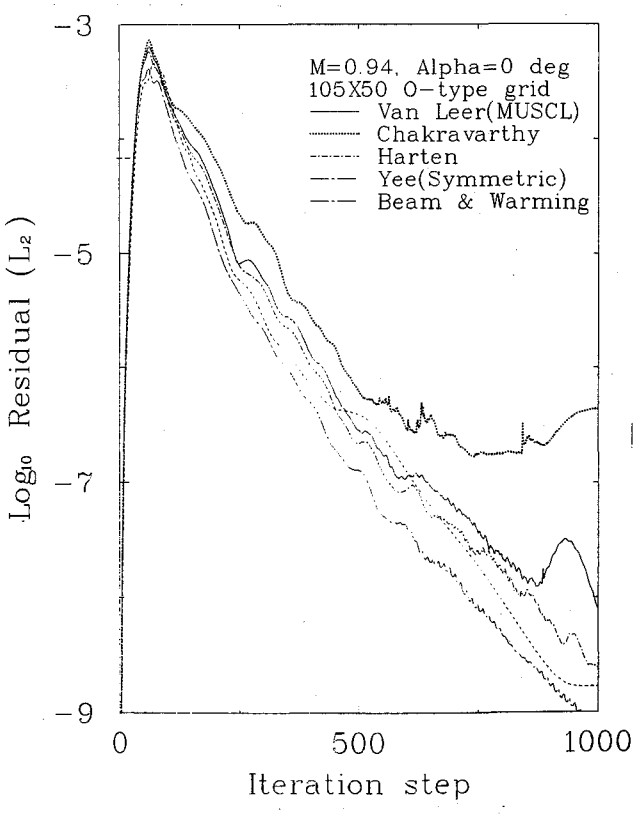

Fig. 9 Mach number contour, $M_\infty = 0.97$, $\alpha = 0$ deg.

than that of Van Leer. The CPU time per iteration per grid point for the Chakravarthy's MUSCL-type scheme is the longest among four TVD schemes.

4-Deg Angle of Attack

There are only two TVD schemes used for comparison to save CPU time for the case of angle of attack: Van Leer's third-order MUSCL-type TVD scheme[9] and Yee's second-order symmetric TVD scheme.[12]

Effect of Different Grids

It is desirable to perform the numerical experiments to investigate the grid sensitivity. Grid systems of $128 \times 60 \times 20$, $108 \times 72 \times 20$, and $108 \times 60 \times 26$ are employed for the verification of the grid independence in the longitudinal, normal, and circumferential directions, respectively. The $128 \times 60 \times 20$ grid has 20 more points inserted on the boat tail ($5.297 < X/D < 5.801$) in the longitudinal direction than the $108 \times 60 \times 20$ grid. The $108 \times 60 \times 26$ grid has 6 more points inserted in the circumferential direction than the $108 \times 72 \times 20$ grid. There are 12 more points inserted in the radial direction in the $108 \times 72 \times 20$ grid than in the $108 \times 60 \times 20$ grid. It is found that the computed surface pressure coeffi-

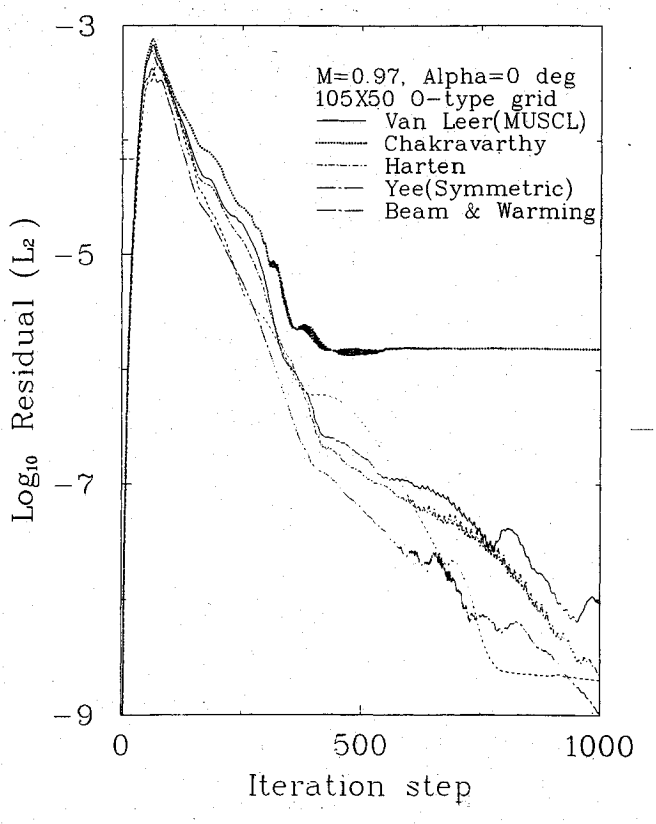

Fig. 10 Iteration histories by different schemes, $M_\infty = 0.94$, $\alpha = 0$ deg.

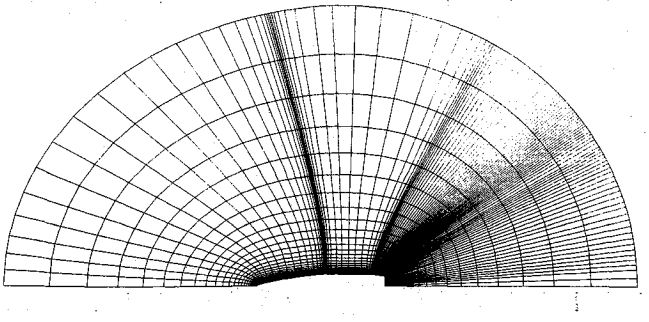

Fig. 11 Iteration histories by different schemes, $M_\infty = 0.97$, $\alpha = 0$ deg.

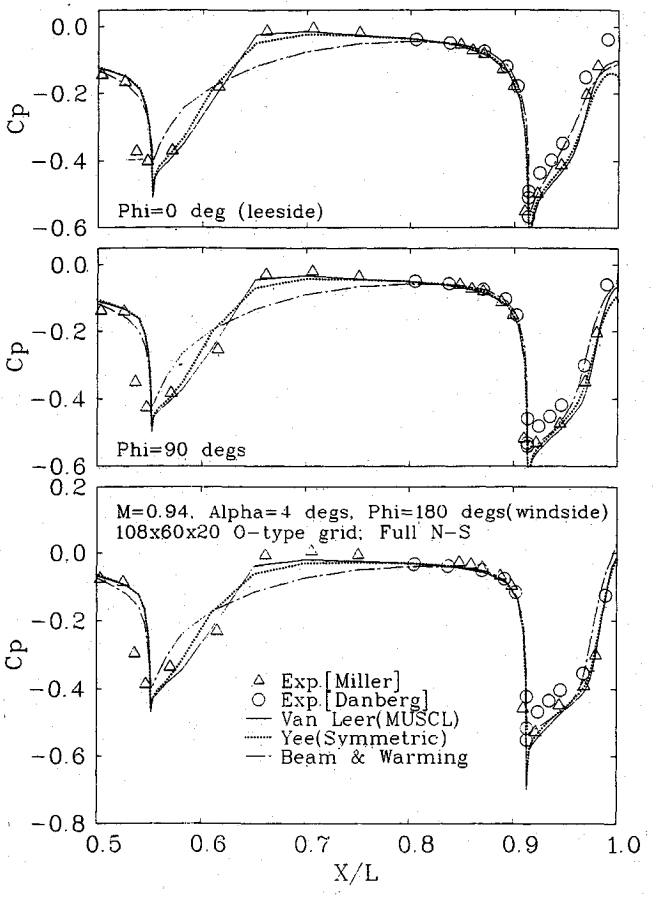

Fig. 12 Surface pressure coefficient distributions by different schemes, $M_\infty = 0.94$, $\alpha = 4$ deg.

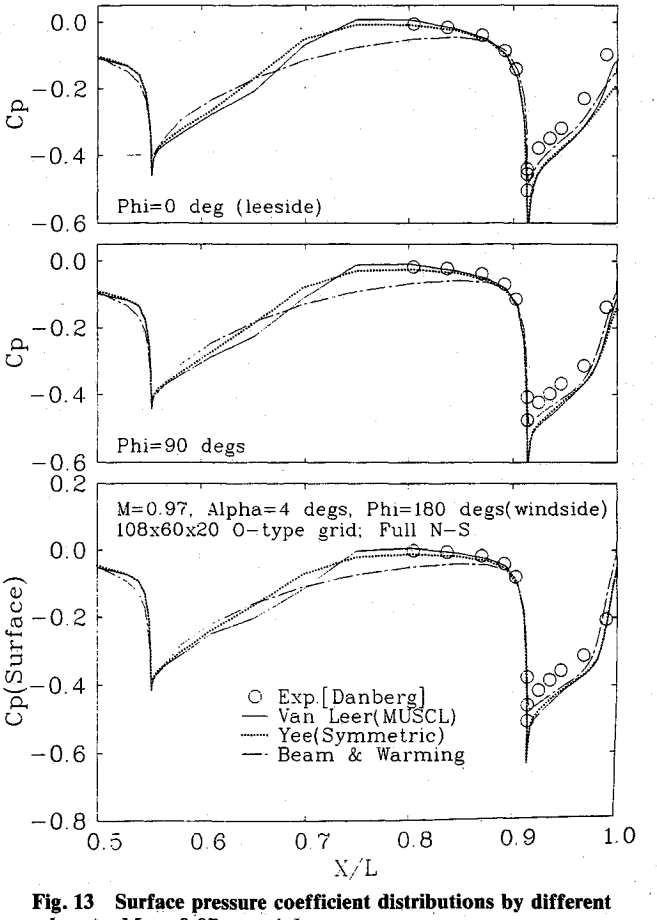

Fig. 13 Surface pressure coefficient distributions by different schemes, $M_\infty = 0.97$, $\alpha = 4$ deg.

Table 1 Computation time for two-dimensional problem

Scheme	CPU s/step/grid point $\times 10^{-4}$
Van Leer's MUSCL	0.708
Chakravarthy's MUSCL	0.755
Harten	0.734
Yee's symmetry	0.707
Beam-Warming	0.684

cients and velocity profiles agree with each other within a maximum 2% difference for these four grids if Van Leer's third-order MUSCL-type TVD scheme is applied. Therefore, the $108 \times 60 \times 20$ grid is chosen as the standard grid system for computations at 4-deg angle of attack.

Comparisons of Different Schemes

Surface pressure coefficient. Figure 12 shows the computed pressure coefficients vs data from Nietubicz et al.[14] and Miller and Molnar[15] employing different schemes for Mach number 0.94 and 4-deg angle of attack. Experimental data of Ref. 15 are available over the entire body and are generally consistent with the data of Ref. 14 in the vicinity of the afterbody. It can be seen that the pressure rise on the boat tail in Ref. 15 is delayed relative to that of Ref. 14, indicating a somewhat more downstream shock position. For Mach number 0.94, the computed results by the two TVD schemes essentially agree with Ref. 15 everywhere except near the base corner on the leeside ($\phi = 0$ deg) and at the nose-cylinder junction on the windside ($\phi = 180$ deg). The symmetric TVD scheme exhibits larger differences at these regions than does the MUSCL-type scheme does. The Beam-Warming scheme yields poor agreement with Ref. 15 data at $0.55 < X/L < 0.85$ but exhibits desirable pressure rise on the boat tail ($0.91 < X/L < 1.0$). It is noted that the longitudinal grid distributions are very coarse at $0.5 < X/L < 0.85$ and fine at $0.91 < X/L < 1.0$. Also, Fig. 12 shows that the results are more sensitive to grid spacings in the Beam-Warming scheme

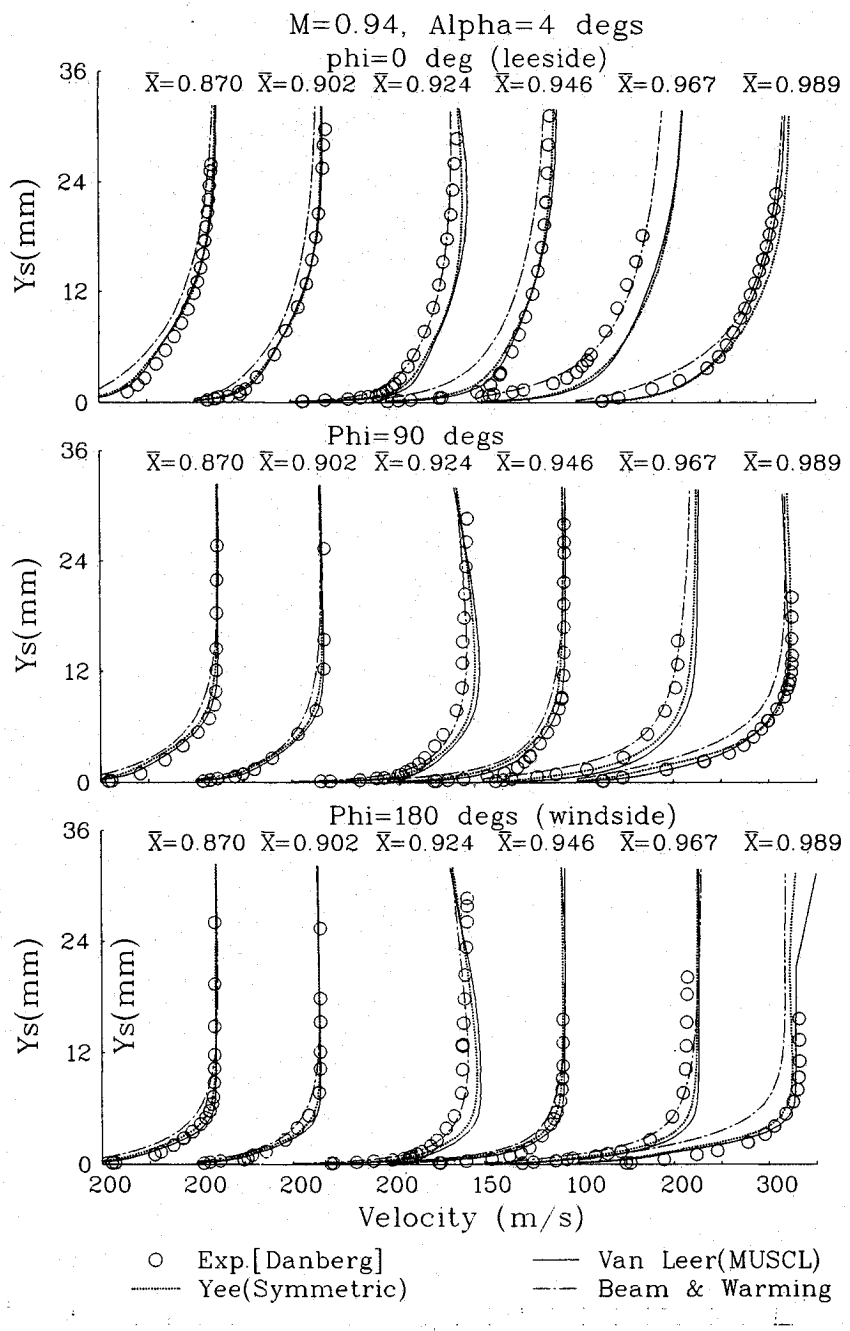

Fig. 14 Velocity profiles at various axial station, $M_\infty = 0.94$, $\alpha = 4$ deg.

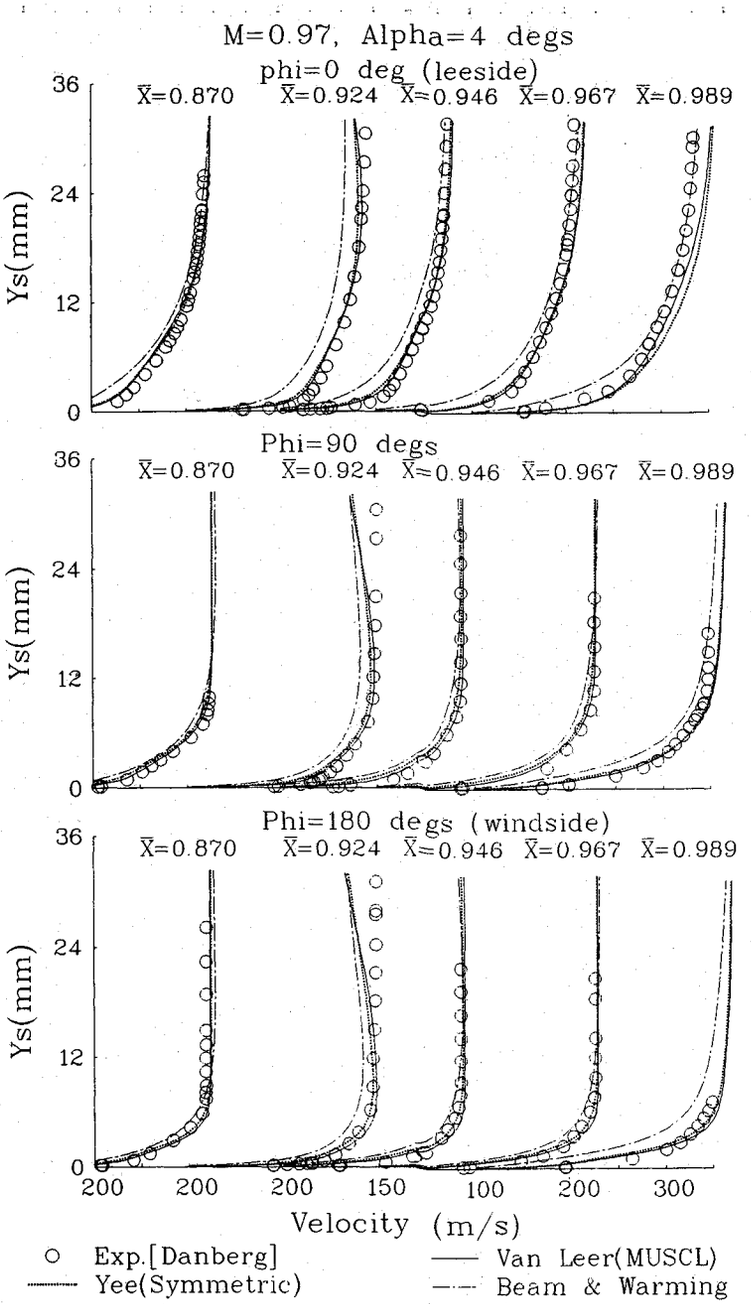

Fig. 15 Velocity profiles at various axial station, $M_\infty = 0.97$, $\alpha = 4$ deg.

than in the TVD schemes as discussed for zero angle of attack. All schemes cannot accurately predict the pressure value at $0.97 < X/L < 1.0$ on the leeside, but Van Leer's third-order scheme gives better results than other two schemes in this region. For Mach number 0.97 (Fig. 6), the data of Ref. 14 are only available at $0.8 < X/L < 1.0$ and the comparisons of computational results by different TVD schemes are similar to the trends of Mach number 0.94. The computed results of the two TVD schemes are very close except for small differences observed in the regions near the base corner on the leeside. All schemes predict pressure coefficients lower than those in Ref. 15, and the Beam-Warming scheme gives slightly higher pressure than do the two TVD schemes on the boat tail region.

Velocity profile. For Mach number 0.94 (Fig. 14), experimental data for velocity profiles at axial stations of $X/L = 0.870$, 0.902, 0.924, 0.946, 0.967, 0.989 can be used for comparison. It can be seen that two TVD schemes exhibit excellent agreement with experimental data at stations $X/L = 0.870$, 0.902, and 0.946, but overestimate the velocity magnitude at $X/L = 0.967$ and 0.989. The discrepancy at stations $X/L = 0.924$ and 0.967 can be explained by the same reasons as for the case of zero angle of attack; i.e., these stations are located near the expansion fan regions and shock (Fig. 18). For the station $X/L = 0.989$, Van Leer's third-order scheme yields very good predictions of the velocity profile. The overestimation and underestimation are observed by the symmetric TVD and the Beam-Warming schemes. The predicted velocities by the Beam-Warming scheme are somewhat lower than those by the TVD schemes at all stations and all three azimuthal angles (i.e., $\phi = 0$, 90, and 180 deg). For Mach number 0.97 (Fig. 15), only data from five stations are available. All TVD schemes yield excellent agreement with measurements at stations $X/L = 0.870$, 0.946, and 0.967 but yield different predictions at stations $X/L = 0.924$ and 0.989. The predicted velocities by the Beam-Warming scheme are lower than those by the two TVD schemes and experimental data of Ref. 14.

Iteration history. The iteration histories for the three schemes are plotted in Figs. 16 and 17. For Mach number 0.94, it is found that the convergent rate by Yee's symmetric

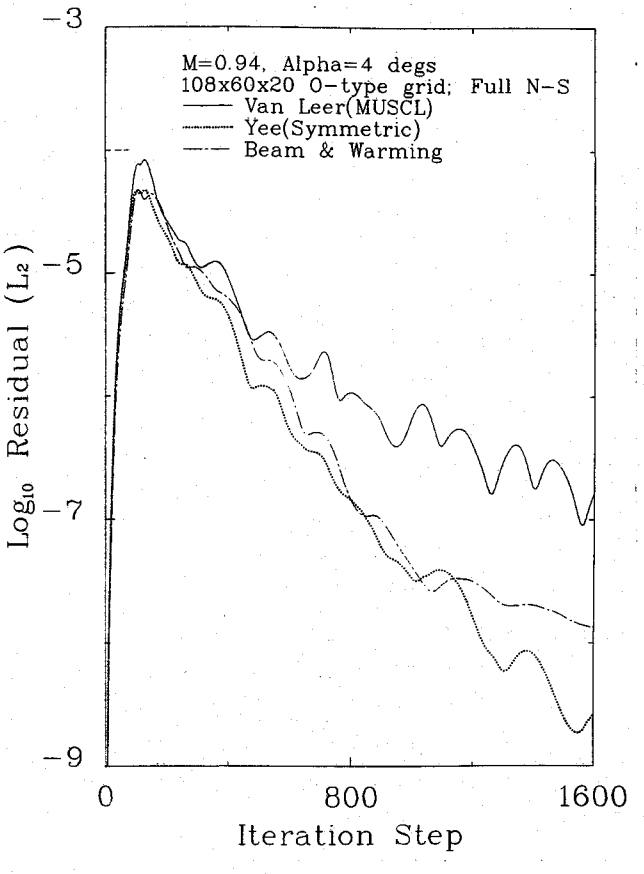

Fig. 16 Iteration histories by different schemes, $M_\infty = 0.94$, $\alpha = 4$ deg.

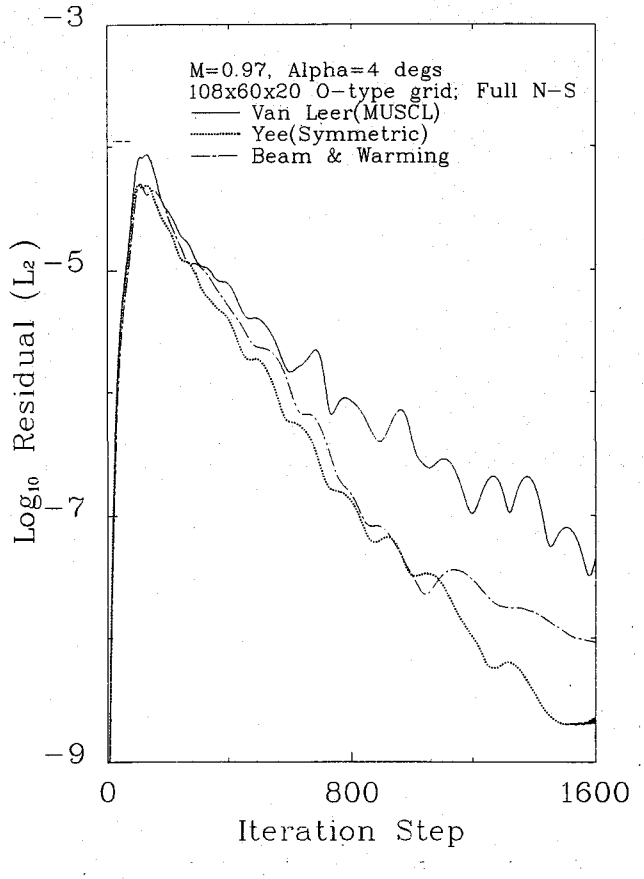

Fig. 17 Iteration histories by different schemes, $M_\infty = 0.97$, $\alpha = 4$ deg.

TVD scheme is the fastest and the residuals can be reduced four orders of magnitude at 1600 iterations. The Beam-Warming scheme converges faster than the third-order MUSCL-type TVD scheme and the residuals can be reduced three orders after 1600 iterations. Van Leer's third-order scheme exhibit larger oscillations than the other two schemes and the residuals cannot be reduced over three orders at 1600 iterations. If the third-order scheme is applied, the pressure coefficients near the base region on the leeside are apparently not changed after 2600 iterations. For Mach number 0.97, the comparisons of the convergence of the three schemes are similar to those for Mach number 0.94. A faster convergence rate can be obtained for Mach number 0.97 than for Mach number 0.94 for all schemes, and the steady solutions by third-order schemes can be achieved after 2000 iterations.

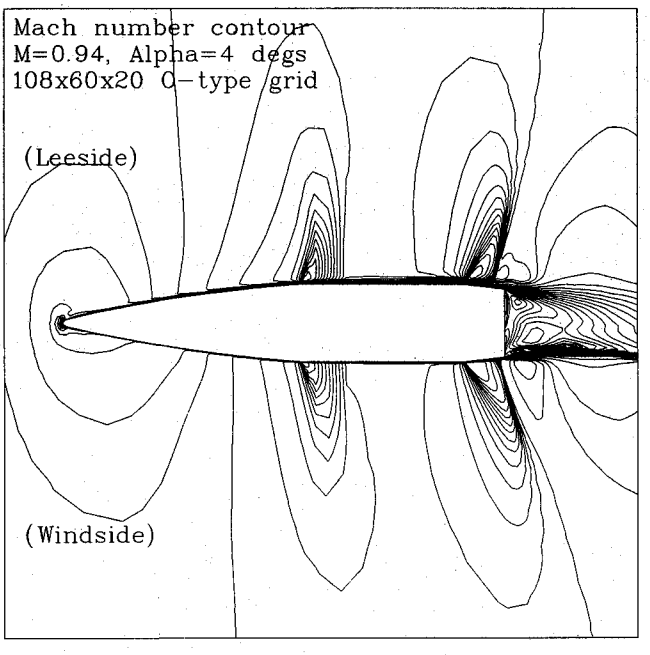

Fig. 18 Mach number contour, $M_\infty = 0.94$, $\alpha = 4$ deg.

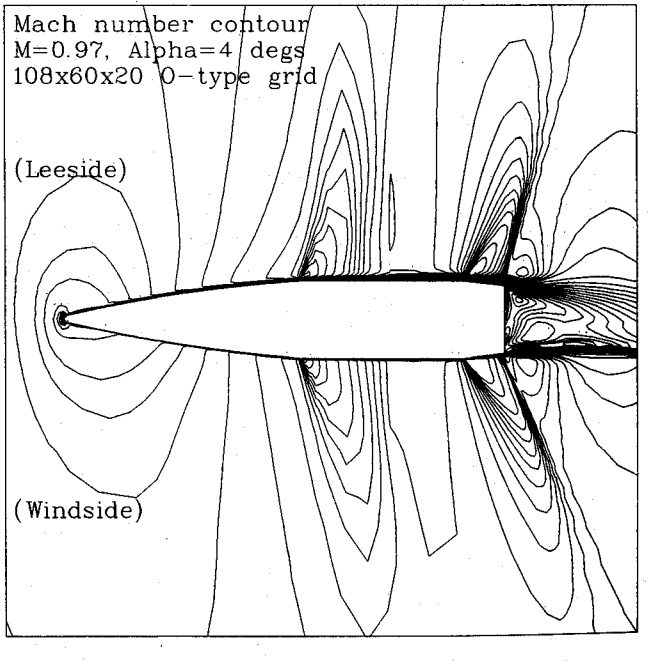

Fig. 19 Mach number contour, $M_\infty = 0.97$, $\alpha = 4$ deg.

Table 2 Computation time for three-dimensional problem

Scheme	CPU s/step/grid point $\times 10^{-4}$
Van Leer's MUSCL	1.123
Yee's symmetry	1.066
Beam-Warming	1.034

Mach number contour. Figures 18 and 19 show the Mach number contours of the projectile for the case of 4-deg angle of attack and Mach numbers of 0.94 and 0.97. These figures show the expansions at the ogive-cylinder and cylinder-boat-tail corners. These figures also indicate the presence of shock waves on the cylinder as well as on the boat tail at transonic speeds. Sharp shocks are observed on the boat tail. These boat tail shocks are shown to be longitudinally asymmetric due to the influence of angle of attack. The asymmetry can also be seen in the wave flow behind the base. As the Mach number is increased from 0.94 to 0.97, the shocks become stronger and move toward the base of the projectile.

CPU time. The three-dimensional computations were performed on the CRAY XMP-14 computer. A total of 2.3×10^6 words of memory were required for the $108 \times 60 \times 20$ grid. The CPU time for the three schemes is given in Table 2. It is found that all CPU times per iteration per grid point for the three-dimensional problem are approximately 40% longer than for the two-dimensional problem. The Beam-Warming scheme requires less computer time than do the TVD schemes. The CPU time per iteration per grid point of Van Leer's third-order MUSCL-type TVD scheme is somewhat longer than that by Yee's second-order symmetry TVD scheme.

Conclusions

A time-dependent two- and three-dimensional Navier-Stokes computer code that incorporated several TVD and Beam-Warming schemes has been developed. Transonic turbulent flows past a real projectile at 0- and 4-deg angle of attack have been computed using O-type grids. Predicted surface pressure distributions and velocity profiles on a boat-tail afterbody agree reasonably well with test data at Mach 0.94 and 0.97. It was found that results using third-order TVD schemes provided slightly better agreement with experimental data than that obtained from second-order TVD schemes. However, slow convergence was observed for higher-order schemes as seen from their iteration histories. In addition, the results using TVD schemes showed general improvements in the shock/boundary-layer interaction region over the basic Beam-Warming method with fixed grid.

Acknowledgment

This study was sponsored by the National Science Council of the Republic of China under Contract NSC-80-0413-E007-11.

References

[1]Beam, R., and Warming, R. F., "An Implicit Factored Scheme for Compressible Navier-Stokes Equations," AIAA Paper 77-645, June 1977.

[2]Pulliam, T. H., and Steger, J. L., "On Implicit Finite-Difference Simulations of Three-Dimensional Flow," *AIAA Journal,* Vol. 18, No. 2, 1980, pp. 159–167.

[3]Shiau, N. H., and Hsu, C. C., "A Diagonalized TVD Scheme for Turbulent Transonic Projectile Aerodynamics Computation," AIAA Paper 88-0217, Jan. 1988.

[4]Hsu, C. C., Shiau, N. H., and Reed, C. W., "Numerical Simulation of Transonic Turbulent Flow Past a Real Projectile," AIAA Paper 88-0218, Jan. 1988.

[5]Sahu, J., "Numerical Computations of Transonic Critical Aerodynamic Behavior," *AIAA Journal,* Vol. 28, No. 5, 1980, pp. 807–816.

[6]Shiau, N. H., and Hsu, C. C., "Numerical Simulation of 3-D Transonic Turbulent Projectile Aerodynamics by TVD Schemes," AIAA Paper 89-0335, Jan. 1989.

[7]Sahu, J., "Three Dimensional Base Flow Calculation for a Projectile at Transonic Velocity," AIAA Paper 86-1051, May 1986.

[8]Chieng, C. C., and Danberg, J. E., "Navier-Stokes Computations for a Transonic Projectile at Angle of Attack and Comparison with Experiment Data," AIAA Paper 88-2584, Jan. 1988.

[9]Van Leer, B., "Towards the Ultimate Conservative Difference Scheme, Part IV," *Journal of Computational Physics,* Vol. 23, No. 2, 1977, pp. 276–299.

[10]Chakravarthy, S. R., and Ota, D. K., "Numerical Issues in Computing Inviscid Supersonic Flow over Conical Delta Wings," AIAA Paper 86-0440, Jan. 1986.

[11]Yee, H. C., and Harten, A., "Implicit TVD Schemes for Hyperbolic Conservation Laws in Curvilinear Coordinates," AIAA Paper 85-1513, July 1985.

[12]Yee, H. C., "Construction of Explicit and Implicit Symmetric TVD Schemes and Their Applications," *Journal of Computational Physics,* Vol. 68, No. 2, 1987, pp. 151–179.

[13]Steger, J. L., and Warming, R. F., "Flux Vector Splitting of the Inviscid Gasdynamic Equations with Application to Finite-Difference Methods," *Journal of Computational Physics,* Vol. 40, No. 2, 1981, pp. 263–293.

[14]Nietubicz, C. J., Inger, G. R., and Danberg, J. E., "A Theoretical and Experimental Investigation of a Transonic Projectile Flow Field," AIAA Paper 82-0101, Jan. 1982.

[15]Miller, M. C., and Molnar, J. W., "Wind Tunnel Measurements of the Induced Surface Pressures on a Spinning Artillery Projectile Model in the Transonic Speed Regime," Chemical Research, Development and Engineering Center, CRDEC-TR-86081, Sept. 1986.

[16]Baldwin, B. S., and Lomax, H., "Thin Layer Approximation and Algebraic Model for Separated Turbulent Flows," AIAA Paper 78-0257, Jan. 1978.

[17]Roe, P. L., "Approximate Riemann Solvers, Parameter Vectors, and Difference Schemes," *Journal of Computational Physics,* Vol. 43, No. 2, 1981, pp. 357–372.

[18]Lin, H., and Chieng, C. C., "Characteristic-Based Flux Limiters of an Essentially Third-Order Flux-Splitting Method for Hyperbolic Conservation Laws," *International Journal for Numerical Methods in Fluids,* Vol. 13, No. 2, 1991, pp. 287–307.

[19]Coakley, T. J., "Turbulence Modeling Methods for the Compressible Navier-Stokes Equations," AIAA Paper 83-1693, July 1983.

[20]Pulliam, T. H., and Steger, J. L., "Recent Improvements in Efficiency, Accuracy, and Convergence for Implicit Approximate Factorization Algorithms," AIAA Paper 85-0360, Jan. 1985.

[21]Steger, J. L., Nietubicz, C. J., and Heavey, K. R., "A General Curvilinear Grid Generation Program for Projectile Configurations," U.S. Army Ballistic Research Laboratory, ARBRL-TR-03142, Aberdeen Proving Ground, MD, Oct. 1981.

[22]Chen, M., Hsu, C. C., and Shyy, W., "Assessment of TVD Schemes for Inviscid and Turbulent Flow Computation," *International Journal for Numerical Methods in Fluids,* Vol. 12, No. 2, 1991, pp. 161–171.